Dalton Transactions

ROYAL SOCIETY OF CHEMISTRY

PAPER

View Article Online
View Journal | View Issue

Cite this: *Dalton Trans.*, 2024, **53**, 13628

$(C_3H_7NH_3)_4Bi_{1-x}Sb_xI_9$: 0D hybrid halide perovskite-like compounds with isolated triiodide units†

Abinash Pradhan,[a] Rajanikanta Rana,[b] Gopalan Rajaraman,[b] Monalisa Pradhan[c] and Saroj L. Samal *[a,d]

Antimony/bismuth-based organic–inorganic hybrid halide perovskite-like compounds have generated enormous research interest due to their excellent optical properties. Exploration of new compounds and understanding of their structural stability and optoelectronic properties is of utmost importance for practical applications of these materials. We report two new 0D perovskite-like compounds and their solid solution, $(C_3H_7NH_3)_4Bi_{1-x}Sb_xI_9$, having propyl amine as the spacer cation and iodine as the halide ion. All compounds crystallized in the space group *C*2/*m* at room temperature and undergo a phase transition from *C*2/*m* to $P2_1/c$ at low temperature (90 K) as observed from the single-crystal study. A low-temperature (250 K, 180 K, 150 K and 90 K) single-crystal study shows that the $(PA)_4BiI_9$ compound retains the monoclinic space group *C*2/*m* until 150 K and undergoes a phase transition to the $P2_1/c$ space group at 90 K. Further, it is observed that ordering, rearrangement and relaxation of the long-chain propyl amine group are primarily responsible for the structural transition. The structure contains $[(Bi/Sb)I_6]^{3-}$ polyhedra along with linear I_3^- units, giving rise to the formula of $(PA)_3(Bi/Sb)I_6{\cdot}(PA)I_3$. The I_3^- units interact poorly while the $[MI_6]^{3-}$ (M = Bi, Sb) octahedral units interact significantly with spacer cations *via* the H-bond, resulting in more distortion in these octahedral units. Theoretical calculations revealed that iodide ions have dual roles and contribute largely to both the valence band maxima and conduction band minima in these compounds. From both experimental and theoretical calculations, it is observed that the pristine compounds are of the indirect band gap-type and Sb substitution in $(PA)_4Bi_{1-x}Sb_xI_9$ led to a gradual decrease in the band gap.

Received 10th June 2024,
Accepted 19th July 2024

DOI: 10.1039/d4dt01692k

rsc.li/dalton

Introduction

Organic–inorganic metal halide perovskites (OIMHPs) are emerging as potential photovoltaic absorber materials because of their excellent optoelectronic properties.[1–8] Some of their unique properties, such as high absorption coefficient, long carrier diffusion length, excellent charge transport, high photoluminescence efficiencies and low deep level trap states, make these compounds potential high-performance optoelectronic devices, such as light-emitting diodes and solar cells.[9–14] After the discovery of the primary compound, methyl ammonium lead iodide ($CH_3NH_3PbI_3$),[15] substantial research activity on $CH_3NH_3PbI_3$ and related compounds led to the improvement of PCE from 3.8% [15] to ~25% within a decade.[16] However, the toxicity of lead as well as the poor stability towards light, heat, and atmospheric moisture of these compounds hinders their practical application in a large scale.[17,18] This scenario has led to search for alternate lead-free hybrid halide perovskite-like compounds containing environmentally friendly elements with enhanced stability.[2,19–21] Among lead-free halide perovskites, Sn/Ge-based halide perovskites[22,23] and Bi/Sb-based defect ordered halide perovskites have been studied the most.[24–26] Bi^{3+}/Sb^{3+}, being isoelectronic with Pb^{2+} and having a 5s/6s lone pair, could be a better replacement for lead.

In the past decade, continuous efforts have been made to understand the structural aspects and chemistry behind the Bi/Sb-based halide perovskites and related compounds because of their structural diversity and unique optical properties.[2,25–28] During our recent study on the hybrid halide

[a]*Solid State and Materials Laboratory, Department of Chemistry, National Institute of Technology, Rourkela-769008, India. E-mail: samalsaroj@nitrkl.ac.in*
[b]*Department of Chemistry, Indian Institute of Technology, Bombay-400076, India*
[c]*Department of Physics, School of Applied Sciences, KIIT Deemed to be University, Bhubaneswar 751024, Odisha, India*
[d]*Center for Nanomaterials, National Institute of Technology, Rourkela-769008, India*

† Electronic supplementary information (ESI) available. CCDC 2309053, 2309067, 2309068, 2309055, 2357506, 2357507, 2357508, 2309056, 2334622, 2309061 and 2309058. For ESI and crystallographic data in CIF or other electronic format see DOI: https://doi.org/10.1039/d4dt01692k

perovskites, $(C_2H_5NH_3)_3Bi_{2-2x}Sb_{2x}I_9$, a structural transition was observed from the 0D hexagonal phase containing isolated dimeric units, $[M_2I_9]^{3-}$ (M = Bi/Sb) to the 1D orthorhombic phase *via* a new monoclinic phase with novel isolated trimeric $[M_3I_{12}]^{3-}$ units.[28] Further exploration in the Bi/Sb-based hybrid halide perovskite with varying A-site cation led to isolation of a new series of compounds with compositions $(C_3H_7NH_3)_4Bi_{1-x}Sb_xI_9$. The detailed structural, optical and electronic properties of these compounds were studied.

Experimental section

Chemicals

$CH_3CH_2CH_2NH_2$ (≥99%; Sigma-Aldrich), Bi_2O_3 (≥99.5%; HiMedia), Sb_2O_3 (≥99.5%; HiMedia), and HI (Hi-AR grade; Sigma-Aldrich) were purchased and used without further purification.

Synthesis

The phase pure crystals of the $(C_3H_7NH_3)_4Bi_{1-x}Sb_xI_9$ series were synthesized by a solution method. Reactants were added to a single-neck round-bottom flask and stirred at 100 °C for 60 min until the formation of a clear solution. Initially, the stoichiometric amount of Bi_2O_3/Sb_2O_3 was taken, followed by the addition of 8 ml of concentrated HI and propyl amine (164 μL) to the round-bottom flask with continuous stirring and heating. A deep-red clear solution was obtained after stirring and heating. It should be noted that Sb-based compounds are soluble at a slightly higher temperature (~100 °C) than Bi compounds (~80 °C). The clear solutions of the synthesized materials were kept in a Petri dish at room temperature for slow evaporation. After 5–10 days, brick-shaped crystals were obtained (Fig. S1 in ESI†) and collected from the solvent for further characterizations.

Characterization techniques

The large deep-red crystals were cut into small pieces. Single-crystal diffraction data were collected at room temperature and low temperature with 0.3° scans in ω and 10 s per frame exposures using a Rigaku XtaLAB Synergy PRO II X-ray diffractometer equipped with a micro-focus sealed X-ray tube Mo-Kα (λ = 0.71073 Å) source and HyPix3000 (CCD plate) detector. CrysAlisPro software was used for data acquisition and data extraction. Empirical absorption corrections were employed using the Scale3 Abspack. The Olex^2 software package associated with the SHELXT program was employed for solving the structure using the intrinsic phasing method. Structure refinement was carried out with the ShelXL software package using least square minimisation. For mixed Bi/Sb compounds, equal displacement parameter (EADP) and equal coordinate (EXYZ) constraints were used, indicating that both atoms share the same crystallographic site. Anisotropic thermal parameters were refined for all the atoms except H atoms. During refinement, lighter elements such as C, N and H showed positional disorder due to larger thermal vibration. In order to solve this issue, these atoms were split into two fragments considering the position of residual electron density (Q peaks). Further, restraints such as RIGU and SIMU were applied on the entire disordered molecule (both the fragments) to fix its position, followed by anisotropic refinement of the whole fragment. The hydrogen atoms of $-CH_3$, $-CH_2$ and $[-NH_3]^+$ groups were generated and fixed geometrically by the appropriate instructions (AFIX 33, and AFIX 23) and refined isotropically with a "riding" model. Detailed crystallographic data and structural refinement parameters are summarized in Tables S1–S47.†

The structural characterization was carried out by powder X-ray diffraction (PXRD) using a Rigaku ULTIMA-IV powder X-ray diffractometer equipped with a Cu-Kα source (λ = 1.5406 Å). The data were collected in the 2θ range of 5°–60° with a step size of 0.02 and scan rate of 3° min^{-1}.

Raman spectra were collected with a confocal micro-Raman spectrometer (Renishaw Invia) using a laser excitation wavelength of 785 nm in a backscattering configuration employing a longworking objective lens (50×, NA = 0.45). The temperature dependent Raman spectra were acquired using a heating-cooling stage (Linkam THMS 600). The laser power on the sample was kept low to avoid local heating. The laser exposure time on the sample was kept fixed for 10 s with two accumulations. Field emission scanning electron microscopy (FESEM) images were acquired using a NOVA NANO SEM/FEI 450 system. The elemental composition was calculated from energy dispersive X-ray (EDX) analysis. For the optical study, a JASCO V-750 spectrophotometer (wavelength range: 200–900 nm) was used. $BaSO_4$ was used as the reference to record the diffuse reflectance spectra (DRS). The band gap was calculated using the Kubelka–Munk equation.[25]

Theoretical study

All theoretical calculations were performed using first-principle density functional theory (DFT) as implemented in the Vienna *Ab initio* Simulation Package (VASP 6.2.0).[29,30] We used the projector augmented wave (PAW)[31] method potentials to describe the interaction between the ion core and valence electrons (electron–ion interactions).[31,32] All calculations were performed using the exchange–correlation potential of Perdew–Burke–Ernzerhof (PBE) parameterization under generalized gradient approximation (GGA).[33,34] For the calculations, the conjugate gradient algorithm with an energy convergence criteria of 10^{-5} eV and forces on each atom set at <0.01 eV Å^{-1}, respectively, were taken into account. The plane-wave basis set energy cut off was set to be 600 eV. The Brillouin zone was sampled with Monkhorst–Pack *k*-point meshes of 16 × 16 × 16 for the density of states (DOS) calculation. In addition, we used the tetrahedron smearing method with a smearing width of 0.2 eV for all DOS calculations.

Results and discussion

Structural description (room-temperature phase)

PA_4BiI_9. The compound $(PA)_4BiI_9$ was initially isolated while attempting to synthesize $PABiI_4$ in a solution method.

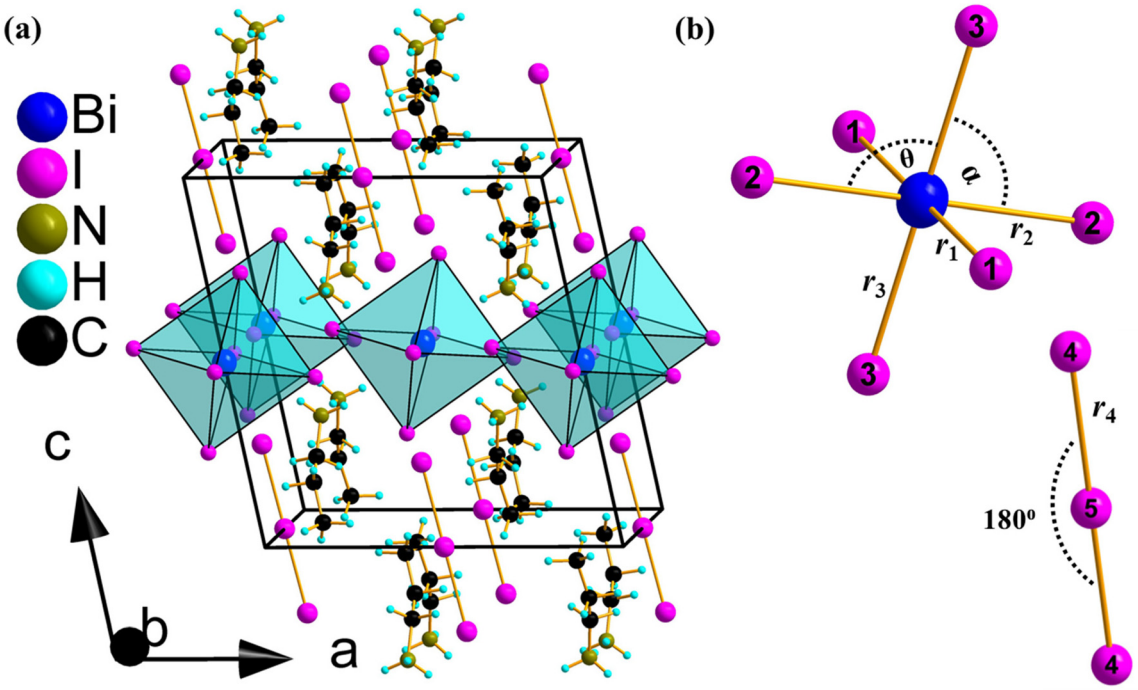

Fig. 1 (a) Crystal structure of PA_4BiI_9 at RT phase. (b) Isolated $[BiI_6]^{3-}$ and $[I_3]^-$ fragments showing Bi–I and I–I bond distances as r_1, r_2, r_3, r_4 and I–Bi–I bond angles as θ and α.

Subsequently, the pure phase was synthesized starting from the stoichiometric amount of reactants. Brick-shaped crystals of $(PA)_4BiI_9$ were isolated and picked for single crystal X-ray diffraction (SCXRD) study. From the SCXRD study, it was found that the compound was crystalized in a monoclinic space group: $C2/m$ (Fig. 1). The lattice parameters were found to be a = 12.0472(4) Å, b = 12.4245(5) Å and c = 12.7142(5) Å. Detail crystallographic information has been provided in Tables S1, S4, S8, S12 and S16 in the ESI.† The structure contains one crystallographic position of Bi (2c) and five crystallographic positions for iodine (three 4i, one 4h and one 2b). The basic building units in the structure are isolated $[BiI_6]^{3-}$ octahedra as observed in 0D halide perovskites and isolated $[I_3]^-$ linear fragments (Fig. 1). In $(PA)_4BiI_9$, propyl amine was a monovalent cation, so the formula could be written as $[(PA)_3BiI_6]\cdot PAI_3$. It may be noted that propyl amine units have a positional disorder, having different occupancies (*e.g.*, 0.7 and 0.3 for C, H and N) in PA_4BiI_9 (Fig. S2†). However, the disordered units are not shown in Fig. 1, and the position of C, N and H with higher occupancy are shown only for the sake of clarity.

The Bi–I bond distance varies from 3.079(1) Å to 3.087(1) Å in the BiI_6 polyhedra, and the I–I distance was 2.939(1) Å in the linear I_3^- fragments (Table 1). The *cis* I–Bi–I bond angle was slightly distorted in the *ac* plane and varied from 88.3° to 91.7° (Table 2) while it has an ideal value (90°) in other planes of the $[BiI_6]$ polyhedra. The distortion of the *cis* I–Bi–I angle in the *ac* plane was attributed to the weak H–bonding (2.74–3.58 Å) of NH_3 protons with the iodide ion of the BiI_6 unit (N–H···I) [Fig. 2(a)].

Table 1 (Bi/Sb)–I bond length of $(C_3H_7NH_3)_4Bi_{1-x}Sb_xI_9$ compounds at room temperature and low temperature

		Bond length (Å)			
	x	r_1	r_2	r_3	r_4
RT phase	0	3.087(1)	3.079(1)	3.079(1)	2.939(1)
	0.23	3.075(1)	3.069(1)	3.068(1)	2.939(1)
	0.62	3.055(1)	3.048(1)	3.044(1)	2.938(1)
	1	3.035(1)	3.027(1)	3.024(1)	2.939(1)
LT (90 K) phase	0	3.078(1)	3.064(1)	3.076(1)	2.939(1)
	0.22	3.068(1)	3.049(1)	3.063(1)	2.938(1)
	0.73	3.038(1)	3.022(1)	3.038(1)	2.940(1)
	1	3.023(1)	3.004(1)	3.024(1)	2.938(1)

PA_4SbI_9. In a similar way, the pristine Sb analogue PA_4SbI_9 was synthesized. It was crystalized in the same monoclinic space group ($C2/m$) as that of $(PA)_4BiI_9$. The lattice parameters were found to be a = 12.0079(7) Å, b = 12.3595(8) Å and c = 12.7066(8) Å which, as expected, were smaller than the Bi-analogue compound. Detailed crystallographic information has been provided in Tables S1, S7, S11, S15 and S19.† This also has a similar structure as PA_4BiI_9, and contains $[I_3]^-$ and $[SbI_6]^{3-}$ units along with propyl amine as the spacer cation. The Sb–I bond varied from 3.024(1) Å to 3.035(1) Å in the SbI_6 unit, and the I–I distance was 2.939(1) Å in the linear fragments I_3 (Table 1). The SbI_6 polyhedra were slightly distorted in the *ac* plane because of weak H-bonding (2.79–3.52 Å) between the NH_3 protons of the propyl amine with the iodide

Table 2 I–(Bi/Sb)–I bond angle of $(C_3H_7NH_3)_4Bi_{1-x}Sb_xI_9$ compounds at room temperature and low temperature

		Bond angle (degree)		
	x	∠I3–(Bi/Sb)–I1 (θ/α)	∠I3–(Bi/Sb)–I2 (θ/α)	∠I1–(Bi/Sb)–I2 (θ/α)
RT phase	0	90/90	91.72(2)/88.28(2)	90/90
	0.23	90/90	91.69(1)/88.31(1)	90/90
	0.62	90/90	91.60(1)/88.40(1)	90/90
	1	90/90	91.59(2)/88.41(2)	90/90
LT (90 K) phase	0	90.26(1)/89.74(1)	91.11(1)/88.89(1)	90.05(1)/89.95(1)
	0.22	90.25(1)/89.75(1)	91.08(1)/88.92(1)	90.02(1)/89.98(1)
	0.73	90.21(1)/89.79(1)	90.96(2)/89.04(2)	90.01(2)/89.99(2)
	1	90.20(1)/89.80(1)	90.88(1)/89.12(1)	90.02(1)/89.98(1)

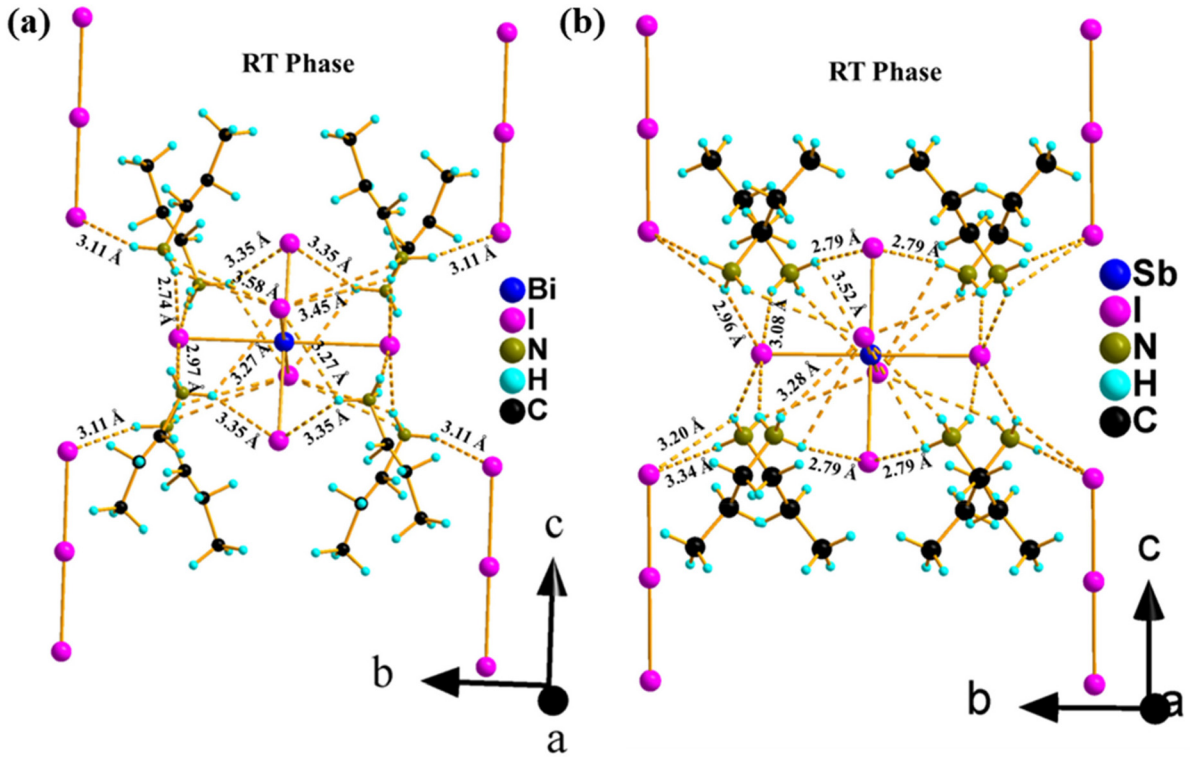

Fig. 2 Crystal structure showing H-bond distances in (a) PA_4BiI_9 (RT phase) and (b) PA_4SbI_9 (RT phase).

ion of the SbI_6 unit (N–H···I) [Fig. 2(b)]. However, the distortion was less in the Sb compound as compared with that in the Bi analogue, as observed from the ∠I–(Bi/Sb)–I bond angle (Table 2). The bond angle was 91.72°/88.28° for PA_4BiI_9 in the *ac* plane and 91.59°/88.41° for PA_4SbI_9. The weak distortion in the Sb compound could be attributed to the relatively weaker H–bonding in PA_4SbI_9 (2.79 Å) than in PA_4BiI_9 (2.74 Å) [Fig. 2(a and b)]. It may be noted that the I–I bond distance in the linear $[I_3]^-$ unit remained unaltered for both Sb and Bi compounds [Fig. 2(b)].

$PA_4Bi_{1-x}Sb_xI_9$. Antimony substitution in $PA_4Bi_{1-x}Sb_xI_9$ with x = 0.25 and 0.75 resulted in composition (refined) of $PA_4Bi_{0.77}Sb_{0.23}I_9$ and $PA_4Bi_{0.38}Sb_{0.62}I_9$. In $PA_4Bi_{1-x}Sb_xI_9$, all the compositions have a similar structure, like the pristine phases, and no phase transition was observed with Sb substitution. The crystallographic details have been provided in ESI Tables S1, S5, S6, S9, S10, S13, S14, S17 and S18.† The MX_6 (M = Bi/Sb) polyhedra remain distorted because of hydrogen bonding (N–H···I) in the whole solid solution. We observed that the polyhedral distortion gradually decreased with Sb substitution at the Bi site in $PA_4Bi_{1-x}Sb_xI_9$. The ∠I–(Bi/Sb)–I bond angle (Table 2) continuously decreased with Sb substitution, which could be attributed to weakening of the H–bond (N–H···I).

Structural analysis of PA_4BiI_9 at different temperatures

In order to understand the phase stability at low temperature, single-crystal data were collected for PA_4BiI_9 compound at four temperatures (*i.e.*, 250 K, 180 K, 150 K and 90 K) and the

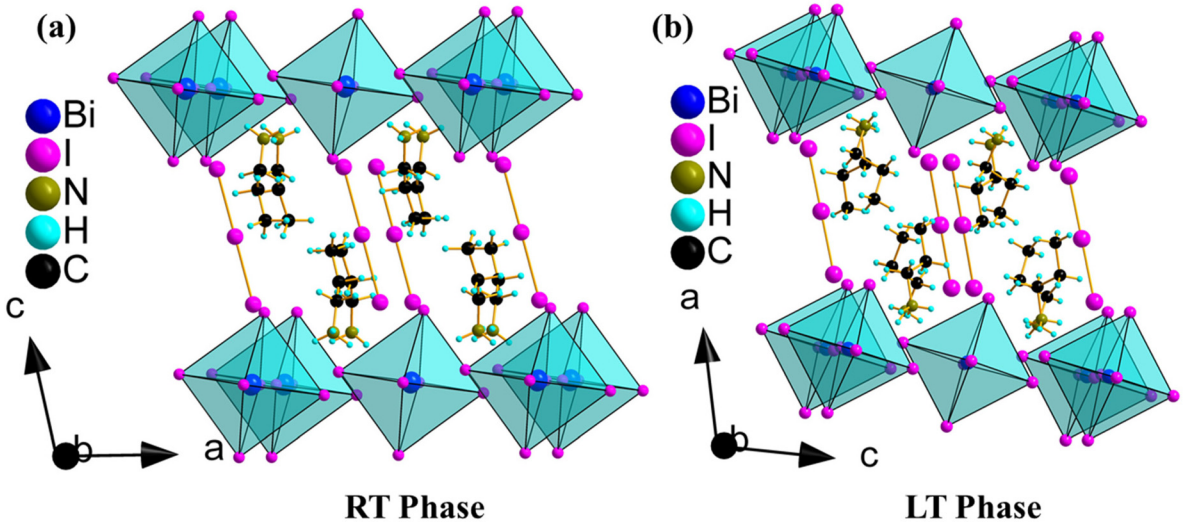

Fig. 3 Crystal structure of PA_4BiI_9 (a) at room temperature (which crystallizes in the *C*2/*m* space group) and (b) at low temperature (90 K) (which crystallizes in the $P2_1/c$ space group).

refined crystallographic data are provided in ESI Tables S3, S4, S8, S12, S16 and S20–S31.† From refinement of the single-crystal structure, we observed that the compound was crystallized in the same space group (*C*2/*m*) as that of RT phase at temperatures of 250 K, 180 K and 150 K. However, all the lattice parameters decreased with a reduction in temperature due to lattice contraction at low temperature. Similarly, the C, N and H atoms of the propyl amine group were disordered at all three temperatures, having an occupancy of 0.49(1)/0.51(1) for 250 K, 0.47(1)/0.53(1) for 180 K and 0.47(1)/0.53(1) for 150 K. When the temperature was decreased further, from 150 K to 90 K, a structural phase transition from *C*2/*m* to $P2_1/c$ was observed. Hence, for all the solid solutions of $(C_3H_7NH_3)_4Bi_{1-x}Sb_xI_9$, the low-temperature single-crystal data were collected at 90 K to observe the phase transition. The details of the low-temperature phase (90 K) for the $(C_3H_7NH_3)_4Bi_{1-x}Sb_xI_9$ compounds are discussed below.

Low-temperature (LT) phase (90 K)

The compound PA_4BiI_9 undergoes a structural phase transition from *C*2/*m* to $P2_1/c$ at low temperature (90 K) (Fig. 3). The lattice parameters were found to be a = 12.5880(4) Å, b = 12.1462(3) Å and c = 11.9457(3) Å. Detailed crystallographic information has been provided in Tables S3, S32, S36, S40 and S44 in ESI.† All the compounds in $PA_4Bi_{1-x}Sb_xI_9$ also undergo a phase transition from *C*2/*m* to $P2_1/c$ at low temperature (90 K), similar to PA_4BiI_9 (Tables S3 and S31–S47†). It may be noted that at low temperature the C-centring lattice was transformed to a primitive lattice type. However, similar to its RT phase, Bi has one crystallographic position (*i.e.*, Bi1 (2b)) and iodine has five positions (one 2c and four 4e each) and possesses the same basic building units. The BiI_6 polyhedra were more distorted than the corresponding RT phase. The I_3^- unit was linear, having a I–I–I bond angle of 180°. The Bi–I bond length of the BiI_6 octahedra ranged from 3.064(1) Å to 3.078(1) Å, and the I–I bond length was 2.939(1) Å in the I_3 linear unit (Table 1). Similarly, the *cis* I–Bi–I bond angles of the BiI_6 unit vary from 88.89(1)° to 91.11(1)° (Table 2). The (Bi/Sb)I_6 polyhedra were more distorted in the LT phase compared with that in the RT phase, as observed from the I–(Bi/Sb)–I bond angle (Table 2). All the I–(Bi/Sb)–I bond angles deviated from the ideal value in the LT phase (Table 2). This phenomenon was due to the formation of relatively stronger H-bonds (Fig. 2) in the LT phase because of the ordering of the organic cation. Further, with Sb substitution in the low-temperature (90 K) phase of $PA_4Bi_{1-x}Sb_xI_9$, the distortion (Table 2) gradually

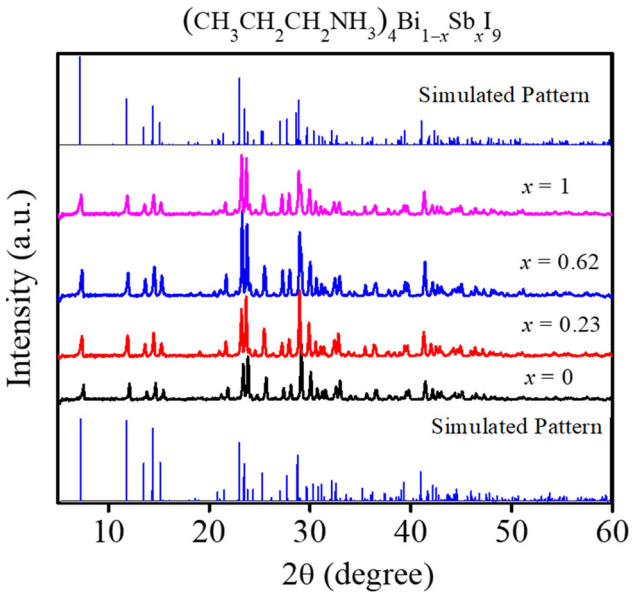

Fig. 4 PXRD pattern of $(C_3H_7NH_3)_4Bi_{1-x}Sb_xI_9$ (x = 0, 0.23, 0.62, 1). The bottom and top patterns are the simulated PXRD patterns obtained from the SCXRD structure solution of PA_4BiI_9 and PA_4SbI_9, respectively.

decreased similar to that seen in the RT phase, which could be attributed to a decrease in the strength of H-bonding. In the LT phase (90 K), the propyl amine unit became ordered and resulted in removal of mirror symmetry along the *ac* plane, which was present in the RT phase (Fig. 2). It may be noted that mirror symmetry was present between two different individual propyl ammonium units in the RT phase, which was removed in the LT phase. Unlike the RT phase, which contains one type of propyl amine unit, the low-temperature phase (90 K) contains two types of propyl amine units. In the RT phase, these units were disordered, having different occupancies (*e.g.*, 0.7 and 0.3 for C, H and N in PA_4BiI_9), while these were ordered in the LT phase (90 K) (Fig. S2 in ESI†). However, for clarity, the disordered units of the RT phase are not shown in Fig. 1–3.

In PA_4MI_9 (M = Bi, Sb), the structural phase transition at low temperature (90 K) was primarily due to the ordering, rearrangement and relaxation of the long-chain propyl amine group. The generation of new crystallographic sites for propyl amine units because of the ordering of the long-chain alkyl amine group could be the reason for the structural transition from $C2/m$ to $P2_1/c$ at low temperature (90 K) in PA_4MI_9 (M = Bi, Sb) compounds.

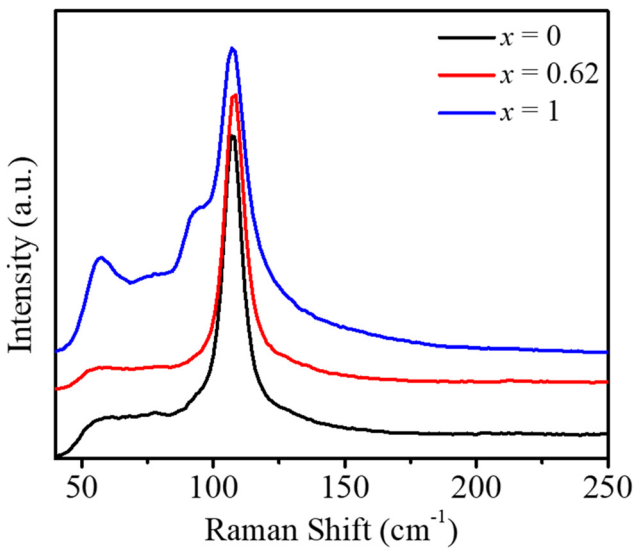

Fig. 5 Room-temperature Raman spectroscopy bands of $(C_3H_7NH_3)_4Bi_{1-x}Sb_xI_9$ (x = 0, 0.62, 1.0).

PXRD study

All the compounds of the $(C_3H_7NH_3)_4Bi_{1-x}Sb_xI_9$ (x = 0, 0.23, 0.62, 1) series were also characterized by powder X-ray diffraction (PXRD) and are shown in Fig. 4. The PXRD data were very well matched with the SCXRD data, confirming the formation of required phases. Further, these compounds were very stable in the ambient condition. To check the stability of the synthesized compounds, PXRD was carried out for all compounds after four months of air exposure, and are shown in Fig. S3 in ESI.† The PXRD data confirmed the retention of the phase and higher stability of the compounds.

Raman spectroscopy

In order to understand the bonding properties in $(C_3H_7NH_3)_4Bi_{1-x}Sb_xI_9$, Raman spectroscopy study was carried out (Fig. 5 and S4†). At room temperature, the samples were scanned from 50 to 3800 cm^{-1}, but the metal–halide bands were observed only within 300 cm^{-1}. For all compounds, one prominent band was visible (a highly intense band) and another one was a low-intensity band. In $(C_3H_7NH_3)_4Bi_{1-x}Sb_xI_9$, the M–I bond lengths of MI_6 octahedra have a very small variation (3.024–3.087 Å) and there are one type of I–I bond distance in the I_3^- unit. The band at around 115 cm^{-1} could be assigned to the symmetric stretching mode

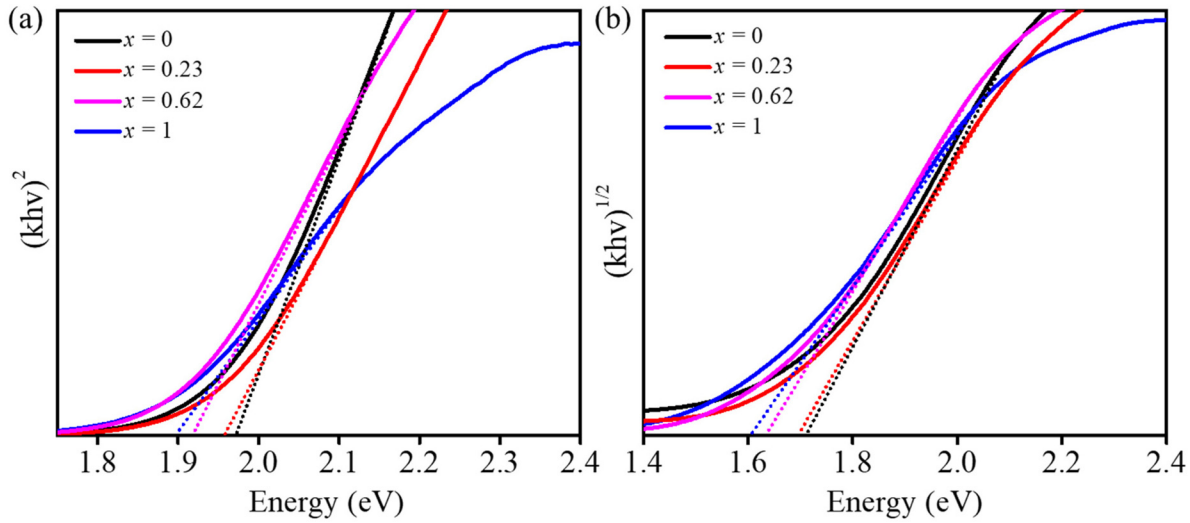

Fig. 6 Tauc plot of $(PA)_4Bi_{1-x}Sb_xI_9$ (x = 0, 0.23, 0.62, 1) showing values of the (a) direct band gap and (b) indirect band gap by extrapolating the slope.

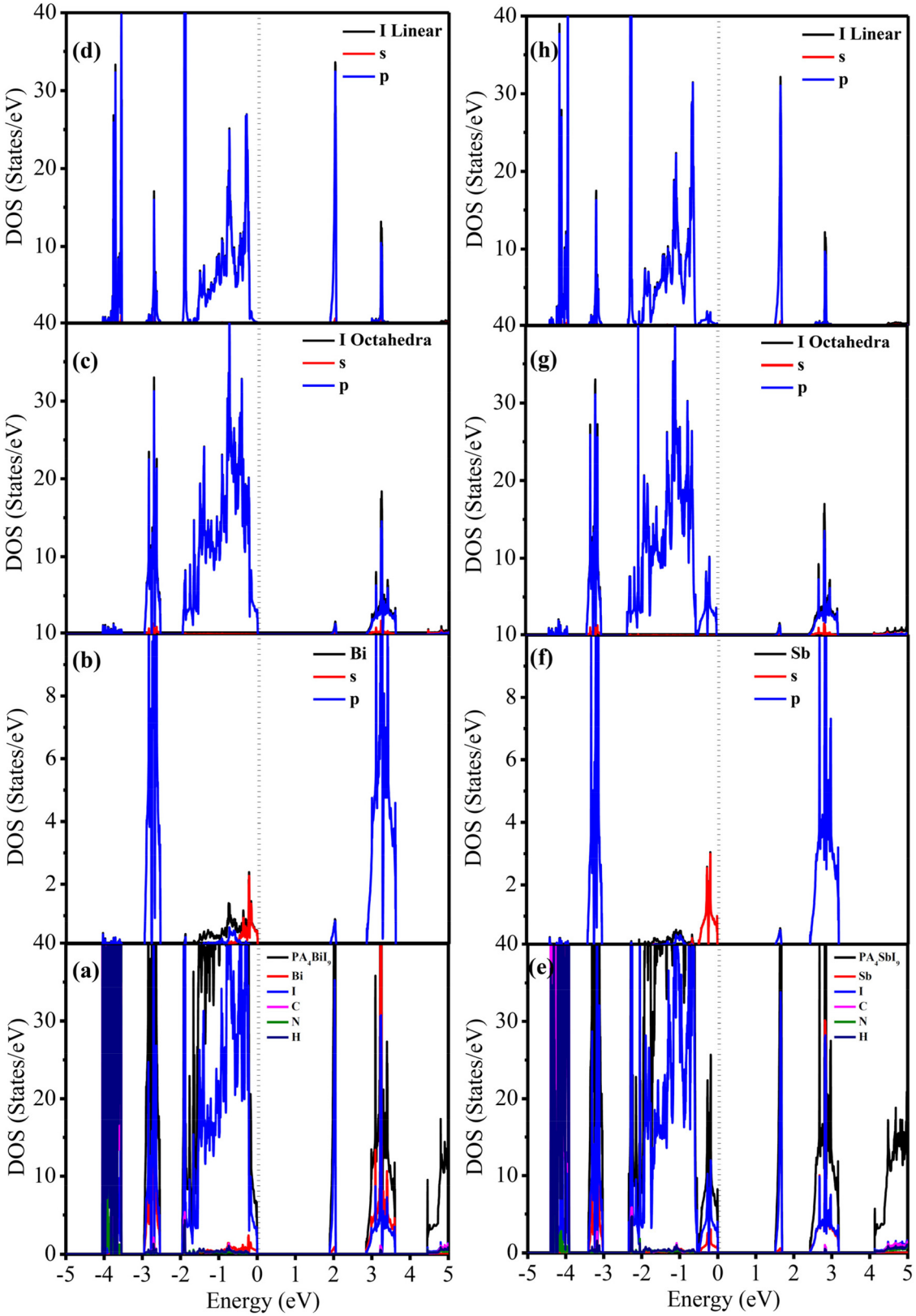

Fig. 7 Densities of states (DOS) calculations for (a–d) PA_4BiI_9 (e–h) PA_4SbI_9. (a and e) Total DOS and DOS for different atom types in PA_4MI_9. Partial projections of orbital components 6s, 6p of the BiI_6 fragment (b) and 5s, 5p of the SbI_6 fragment (f). Partial projections for the 6s, 6p orbital of the octahedral I fragment (c and g) and partial projections for the 6s, 6p orbital of the linear I fragment (d and h).

of vibration of the M–I bond of MI_6 octahedra.[35] The lower frequency mode at ~100 cm^{-1} could be assigned as I_3^--type elementary blocks, as reported previously.[36] Further, from the low-temperature Raman spectroscopy data (collected from 83 K to 298 K) of the pristine Bi compound (Fig. S4 in ESI†), we observed that the prominent band gradually shifted to higher frequency, indicating the contraction of the unit cell with a decrease in temperature.

FESEM and EDX study

The FESEM micrographs of selected compositions from $PA_4Bi_{1-x}Sb_xI_9$ are shown in Fig. S5 of ESI.† Irregularly shaped grains were observed for all compositions. The elemental composition of some selected compounds from the $PA_4Bi_{1-x}Sb_xI_9$ series was determined using FESEM–EDX (Fig. S6–S9†). The elemental mapping is provided in Fig. S6–S9 in ESI.† The composition obtained from FESEM–EDX was well matched with the refined single-crystal composition for each selected compound.

UV-visible diffuse reflectance study

The optical band gap of the synthesized compounds was studied using UV-visible diffuse reflectance study. The DR study was carried out on powder samples of $(C_3H_7NH_3)_4Bi_{1-x}Sb_xI_9$ (x = 0, 0.23, 0.62, 1) (Fig. 6). The Kubelka–Munk equation [$k = (1-R)^2/2R$, where R is the reflectance and k is the absorption coefficient] is used to calculate the pseudo absorbance spectra from reflectance spectra. To calculate the direct and indirect band gap of a material, the equation $(kh\nu)^{1/n} = C(h\nu - E_g)$ (where h is Planck's constant, C is the proportionality constant, ν is the frequency of light, E_g is the band gap, and n is 2 or $\frac{1}{2}$, expressing the indirect or direct band gap of the substance, respectively) is used. Fig. 6(a) and (b) show a plot of $(kh\nu)^{1/n}$ *vs.* $h\nu$ with n = 2 and $\frac{1}{2}$, from which the indirect and direct band gap of the material can be obtained. We observed that the indirect band gap was lower as compared with the direct band gap values for $(PA)_4Bi_{1-x}Sb_xI_9$, which suggests that all the compounds are of the indirect type of band gap. These data corroborated the theoretical data (see Theoretical section).

Furthermore, the indirect band gap of $(PA)_4BiI_9$ is 1.71 eV, which decreases with Sb substitution, and the pristine Sb compound has a band gap of 1.60 eV. The variation of band gap with Sb substitution is rationalized in the Theoretical section.

Theoretical study

In order to understand the electronic properties of these compounds, a theoretical study was carried out using VASP. Density of state (DOS) calculations were performed on the ordered low-temperature phase of PA_4MI_9 (M = Bi, Sb). The total and atom decomposed DOS for PA_4MI_9 (M = Bi, Sb) are shown in Fig. 7. Both compounds showed similar features. Two unique features of these compounds were observed from the DOS analysis. First, the valence band of PA_4MI_9 compounds was contributed largely from the I-p bands of BiI_6/SbI_6 fragments, I-p bands of I_3^- units and Bi/Sb-s band, whereas the conduction band was largely contributed from the I-p bands of I_3^- units. Second, the octahedral iodine was more dispersed due to strong interaction with Sb/Bi, whereas the linear iodine had comparatively localized bands showing a weak interacting nature. It may be noted that, in most Bi/Sb-based halide perovskite-like compounds, the valence band is largely contributed from filled halide-p states, while the conduction band is contributed from the empty (Sb/Bi)-p state.[25,26] However, in PA_4MI_9 (M = Bi, Sb), both the valence band and conduction band are largely contributed from the I-p states.

The band gap was observed to decrease with Sb substitution in $(PA)_4Bi_{1-x}Sb_xI_9$ (Fig. 6). As mentioned in an earlier section, the valence band is largely contributed from the p-states of iodine and (to a lesser extent) s-states of Bi/Sb, while the conduction band is purely from the p-states of iodine from the I_3^-

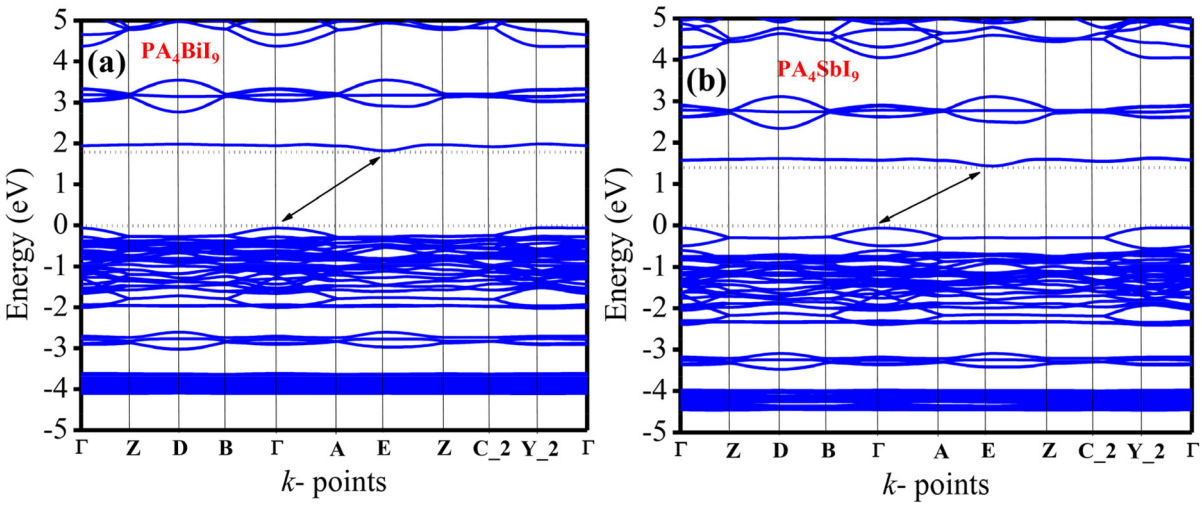

Fig. 8 Band structure of (a) PA_4BiI_9 (b) PA_4SbI_9.

fragment. Hence, there was no change in the conduction band with Sb substitution in $(PA)_4Bi_{1-x}Sb_xI_9$. The change in band gap value was purely due to changes in the valence band with Sb substitution in $(PA)_4Bi_{1-x}Sb_xI_9$.

It may be noted that, unlike other Bi/Sb-based halide compounds, in which the conduction band is largely contributed from the p-states of Bi/Sb, in $(PA)_4Bi_{1-x}Sb_xI_9$ compounds, the conduction band is purely from the p-states of iodine from linear I_3^-. Further, in most Bi/Sb-based halide perovskite-related compounds, the decrease in band gap for the Sb compound is attributed to the low-lying Sb-p states as compared with Bi-p states at the conduction band.[26] However, in these $(PA)_4Bi_{1-x}Sb_xI_9$ compounds, the reason for the decrease in the band gap with Sb substitution was different than the usual case. From the DOS analysis it was observed that in $(PA)_4SbI_9$ there was a significant contribution of the Sb-s state towards the valence band as compared with the Bi-s state of the corresponding Bi-analogue (Fig. 7b and f). Hence, the significant contribution of Sb-s states at the Fermi was responsible for the decrease in band gap in Sb compound.

The band-structure analysis of PA_4BiI_9 indicated the valence band maximum was at the Γ point and the conduction band minimum was at the E point, indicating materials of an indirect band gap-type [Fig. 8(a)] and corroborated the observed indirect band gap-type from the UV-visible DR study. Similar behaviour of the DOS and band structure were also observed in the case of PA_4SbI_9 [Fig. 8(b)], making both the Bi and Sb analogues as indirect band gap-type material.

The theoretical band gap values of PA_4BiI_9 and PA_4SbI_9 were 1.86 eV and 1.48 eV, respectively, which were very close to the experimentally observed band gap of the corresponding compounds (1.71 eV and 1.60 eV for PA_4BiI_9 and PA_4SbI_9, respectively). Further, for both compounds, a nearly flat band was observed (Fig. 8), which was attributed to the isolated nature of the inorganic moieties. The flat bands in these compounds resulted in substantially larger carrier effective mass.

Conclusions

In summary, we synthesized two new halide perovskite-like compounds, $(PA)_4MI_9$ (M = Bi/Sb), and their solid solution containing isolated $[MI_6]^{3-}$ octahedra and I_3^- linear units. The molecular formula could be written as $(PA)_3MI_6{\cdot}(PA)I_3$. Analysis of single-crystal data on $(PA)_4BiI_9$ compound (at 250 K, 180 K, 150 K and 90 K) indicated that the compound retained the monoclinic $C2/m$ space group until 150 K, and a structural phase transition was observed from space group $C2/m$ to $P2_1/c$ at 90 K. Further, all compounds in $(PA)_4Bi_{1-x}Sb_xI_9$ showed a structural phase transition from space group $C2/m$ to $P2_1/c$ at 90 K as evident from the single-crystal study. Theoretical calculations revealed that iodide ions had dual roles and contributed largely to both the valence band maxima (I-p states of the $[MI_6]^{3-}$ octahedra) and almost completely to the conduction band minima (I-p states of the $[I_3]^-$ linear fragment) in these compounds. From the calculations of electronic band structure, it was observed that both compounds were of the indirect band gap-type. Substitution of Sb in $(PA)_4Bi_{1-x}Sb_xI_9$ led to a reduction in the band gap, which was attributed to the significant contribution of the Sb-s state in addition to the I-p states of $[SbI_6]^{3-}$ towards the valence band maximum.

Data availability

Crystallographic data for $(PA)_4Bi_{1-x}Sb_xI_9$ [x = 0 (293 K), 0.23 (293 K), 0.62 (293 K), 1 (293 K), 0 (250 K), 0 (180 K), 0 (150 K), 0 (90 K), 0.22 (90 K), 0.73 (90 K), 1 (90 K)] have been deposited at the CCDC under 2309053, 2309067, 2309068, 2309055, 2357506, 2357507, 2357508, 2309056, 2334622, 2309061, and 2309058.†

Conflicts of interest

There are no conflicts to declare.

Acknowledgements

Saroj L. Samal acknowledges the financial support received from the CSIR, Government of India, through 01(3072)/21/EMR-II as an extramural grant. SLS and AP acknowledge the Departmental Single Crystal XRD Facility funded by the DST-FIST (SR/FST/CS-II/2017/34) and the Central Research Facility (CRF) NIT Rourkela for FESEM, Raman and PXRD facilities.

References

1 F. Jiang, D. Yang, Y. Jiang, T. Liu, X. Zhao, Y. Ming, B. Luo, F. Qin, J. Fan, H. Han, L. Zhang and Y. Zhou, *J. Am. Chem. Soc.*, 2018, **140**, 1019–1027.
2 S. S. Das, A. Pradhan and S. L. Samal, *Dalton Trans.*, 2023, **52**, 1777–1784.
3 S. Chatterjee and A. J. Pal, *ACS Appl. Mater. Interfaces*, 2018, **10**, 35194–35205.
4 C. Lan, G. Liang, S. Zhao, H. Lan, H. Peng, D. Zhang, H. Sun, J. Luo and P. Fan, *Sol. Energy*, 2019, **177**, 501–507.
5 J.-C. Hebig, I. Kühn, J. Flohre and T. Kirchartz, *ACS Energy Lett.*, 2016, **1**, 309–314.
6 W. Li, D. Xin, S. Tie, J. Ren, S. Dong, L. Lei, X. Zheng, Y. Zhao and W.-H. Zhang, *J. Phys. Chem. Lett.*, 2021, **12**, 1778–1785.
7 C. Ni, G. Hedley, J. Payne, V. Svrcek, C. McDonald, L. K. Jagadamma, P. Edwards, R. Martin, G. Jain, D. Carolan, D. Mariotti, P. Maguire, I. Samuel and J. Irvine, *Nat. Commun.*, 2017, **8**, 170.
8 G. Zhang, M. Zhu, J. Guan, X. Liu, T. Zeng and W. Yang, *ACS Appl. Energy Mater.*, 2022, **5**, 2738–2746.

9 S. Il Seok, M. Grätzel and N.-G. Park, *Small*, 2018, **14**, 1704177.
10 L. Meng, E. Yao, Z. Hong, H. Chen, P. Sun, Z. Yang, G. Li and Y. Yang, *Adv. Mater.*, 2017, **29**, 1603826.
11 S. D. Stranks and H. J. Snaith, *Nat. Nanotechnol.*, 2015, **10**, 391–402.
12 J. S. Manser, J. A. Christians and P. V. Kamat, *Chem. Rev.*, 2016, **116**, 12956–13008.
13 M. A. Green, A. Ho-Baillie and H. J. Snaith, *Nat. Photonics*, 2014, **8**, 506–514.
14 B. Saparov and D. B. Mitzi, *Chem. Rev.*, 2016, **116**, 4558–4596.
15 A. Kojima, K. Teshima, Y. Shirai and T. Miyasaka, *J. Am. Chem. Soc.*, 2009, **131**, 6050–6051.
16 J. Jeong, M. Kim, J. Seo, H. Lu, P. Ahlawat, A. Mishra, Y. Yang, M. A. Hope, F. T. Eickemeyer, M. Kim, Y. J. Yoon, I. W. Choi, B. P. Darwich, S. J. Choi, Y. Jo, J. H. Lee, B. Walker, S. M. Zakeeruddin, L. Emsley, U. Rothlisberger, A. Hagfeldt, D. S. Kim, M. Grätzel and J. Y. Kim, *Nature*, 2021, **592**, 381–385.
17 S. Zou, Y. Liu, J. Li, C. Liu, R. Feng, F. Jiang, Y. Li, J. Song, H. Zeng, M. Hong and X. Chen, *J. Am. Chem. Soc.*, 2017, **139**, 11443–11450.
18 Y. Wei, W. Wang, Z. Wang, H. Yang, X. You, Y. Zhao, P. Dang, H. Lian, J. Hao, G. Li and J. Lin, *Adv. Funct. Mater.*, 2023, **33**, 2205829.
19 P. Cheng, L. Feng, Y. Liu, D. Zheng, Y. Sang, W. Zhao, Y. Yang, S. Yang, D. Wei, G. Wang and K. Han, *Angew. Chem., Int. Ed.*, 2020, **59**, 21414–21418.
20 K. Kundu, P. Dutta, P. Acharyya and K. Biswas, *J. Phys. Chem. C*, 2021, **125**, 4720–4729.
21 P. Han, C. Luo, S. Yang, Y. Yang, W. Deng and K. Han, *Angew. Chem., Int. Ed.*, 2020, **59**, 12709–12713.
22 T. Krishnamoorthy, H. Ding, C. Yan, W. L. Leong, T. Baikie, Z. Zhang, M. Sherburne, S. Li, M. Asta, N. Mathews and S. G. Mhaisalkar, *J. Mater. Chem. A*, 2015, **3**, 23829–23832.
23 C. Kang, H. Rao, Y. Fang, J. Zeng, Z. Pan and X. Zhong, *Angew. Chem., Int. Ed.*, 2021, **60**, 660–665.
24 K. Kundu, P. Acharyya, K. Maji, R. Sasmal, S. S. Agasti and K. Biswas, *Angew. Chem.*, 2020, **132**, 13193–13200.
25 A. Pradhan, M. K. Jena and S. L. Samal, *ACS Appl. Energy Mater.*, 2022, **5**, 6952–6961.
26 A. Pradhan, S. C. Sahoo, A. K. Sahu and S. L. Samal, *Cryst. Growth Des.*, 2020, **20**, 3386–3395.
27 A. Pradhan, S. Sahoo and S. L. Samal, *CrystEngComm*, 2024, **26**, 312–323.
28 A. Pradhan and S. L. Samal, *Inorg. Chem.*, 2023, **62**, 13802–13811.
29 G. Kresse and J. Furthmüller, *Phys. Rev. B: Condens. Matter Mater. Phys.*, 1996, **54**, 11169–11186.
30 Y. Chen, F. Peng, Y. Yan, Z. Wang, C. Sun and Y. Ma, *J. Phys. Chem. C*, 2013, **117**, 13879–13886.
31 G. Kresse and D. Joubert, *Phys. Rev. B: Condens. Matter Mater. Phys.*, 1999, **59**, 1758–1775.
32 P. E. Blöchl, *Phys. Rev. B: Condens. Matter Mater. Phys.*, 1994, **50**, 17953–17979.
33 J. P. Perdew, K. Burke and M. Ernzerhof, *Phys. Rev. Lett.*, 1996, **77**, 3865–3868.
34 J. Hafner, *J. Comput. Chem.*, 2008, **29**, 2044–2078.
35 N. Elfaleh, H. Chouaib, S. Kamoun and M. P. F. Graça, *J. Phys. Org. Chem.*, 2015, **28**, 674–680.
36 A. A. Tonkikh, D. V. Rybkovskiy and E. D. Obraztsova, *J. Phys. Chem. C*, 2023, **127**, 3005–3012.